Journal of Materials Research and Technology 30 (2024) 9337–9342

Contents lists available at ScienceDirect

Journal of Materials Research and Technology

journal homepage: www.elsevier.com/locate/jmrt

A comprehensive exploration of PPS/MgO@MoS_2 core–shell composites for enhanced thermal and mechanical performance

Minsu Kim [a], Dabin Park [c], Jooheon Kim [a,b,*]

[a] Department of Chemical Engineering, Chung-Ang University, Seoul, 06974, Republic of Korea
[b] Department of Intelligent Energy and Industry, Graduate School, Chung-Ang University, Seoul, 06974, Republic of Korea
[c] Department of Mechanical and Aerospace Engineering, University of California, Irvine, CA, 92679, USA

ARTICLE INFO

Handling Editor: SN Monteiro

Keywords:
Polyphenylene sulfide
Magnesium oxide
Molybdenum sulfide
Core–shell structure
Thermal conductivity

ABSTRACT

The growing worldwide energy crisis and environmental issues have prompted the exploration of sustainable alternatives across different sectors, such as the automotive realm. Electric vehicles (EVs) have surfaced as a practical substitute for traditional fossil fuel-driven vehicles, with their efficacy being contingent upon the weight of the vehicle. In this investigation, we present polyphenylene sulfide (PPS) as an advanced engineering plastic, boasting exceptional resistance to high temperatures and chemical stability. Its versatility makes it suitable for a range of applications within the automotive industry. However, the thermal conductivity of PPS is lower than those of other engineering plastics. Therefore, a novel core–shell structure comprising magnesium oxide (MgO) and molybdenum sulfide (MoS_2) was fabricated to enhance the thermal and mechanical properties. The core–shell structure was elucidated via a comprehensive analysis using various techniques. Furthermore, the PPS/MgO@MoS_2/PA composites were synthesized to address the challenges associated with high filler ratios. Tensile strength evaluations and thermal conductivity assessments confirmed the effectiveness of the proposed materials for diverse engineering applications, particularly in EVs. Additionally, surface treatments with polyformaldehyde and (3-aminopropyl)triethoxysilane (PA) improved the adhesion with the PPS matrix, which enhanced the mechanical tensile strength to 90 MPa. As the filler ratio increased, the MgO@MoS_2 core–shell achieved a high through-plane heat conductivity of 4.07 W/m·K, which is 22 times compared to pristine PPS. Hence, this study provides valuable insights into the ongoing pursuit of sustainable automotive solutions by addressing the critical issues of energy efficiency, environmental impact, and materials science.

1. Introduction

The ongoing global energy crisis and its impact on carbon emissions pose a significant challenge. As a result, Electric automobiles (EVs) are garnering substantial attention in the automobile sector as credible alternatives to traditional fuel sources-powered vehicles. The efficiency of EVs, particularly in terms of fuel efficiency, is closely linked to the weight of their vehicle chassis. Consequently, there is a growing interest in identifying robust materials capable of replacing current components, thereby reducing overall vehicle weight and improving overall efficiency. Engineering plastics (EPs) have emerged as promising contenders in various industries, including automotive, due to their attractive qualities, such as cost-effectiveness, lightweight nature, ease of processing, and resistance to water.

However, their widespread application of EPs has been hindered by several drawbacks. For instance, polycarbonate exhibits poor chemical stability [1,2], polyamide has high moisture absorption [3,4], polybutylene terephthalate (PBT) is prone to hydrolysis when subjected to high-temperature molding [5,6], and polyvinyl chloride (PVC) and polyurethane are vulnerable to low and high temperatures [7,8]. These limitations restrict the widespread application of EPs in various fields. Polyphenylene sulfide (PPS) has emerged as an outstanding super-engineering plastic that can maintain chemical resistance, have dimensional stability and even withstand high temperature. The melting point of PPS (approximately 275 °C) is higher than melting points of other EPs, thus making it an attractive applicant for various applications.

However, PPS exhibits a major disadvantage attributed to a considerably lower thermal conductivity value than that of other EPs. To address this issue, researchers have investigated the integration of

* Corresponding author. Department of Chemical Engineering, Chung-Ang University, Seoul, 06974, Republic of Korea.
E-mail address: jooheonkim@cau.ac.kr (J. Kim).

https://doi.org/10.1016/j.jmrt.2024.06.021
Received 28 March 2024; Received in revised form 20 May 2024; Accepted 4 June 2024
Available online 4 June 2024
2238-7854/© 2024 The Authors. Published by Elsevier B.V. This is an open access article under the CC BY-NC-ND license (http://creativecommons.org/licenses/by-nc-nd/4.0/).

ceramic fillers such as boron nitride (BN) [9–11], aluminum oxide or nitride (Al_2O_3 or AlN) [11–13], and carbon materials [14,15] into the PPS to enhance its thermal and mechanical properties. Our group previously reported PPS/glass fiber composites with MPTMS treated GO and polysiloxide-coated aggregated BN achieved 1.18 W/m·K [16]. Tantug et al. reported 50% synthetic graphite loaded PPS composite showed through-plane thermal conductivity of 1.65 W/m·K, which is 4.7 times that of PPS [17]. Shi et al. reported polydopamine treated PPS/PDA-CNTs-SiC composite shows thermal conductivity of about 1 W/m·K with 22% filler ratio [18]. However, thermal conductivity of PPS composites need to be more improved.

In this study, we focused on environmentally-friendly magnesium oxide (MgO) and molybdenum sulfide (MoS_2) to improve the thermal and mechanical properties of PPS. MgO exhibits several advantages, such as high thermal conductivity of 30–60 W/m·K, thermal stability at high temperatures, and high electrical resistivity; hence, it can be utilized for heat removal from various electronic devices. However, MgO has poor mechanical properties, which should be improved before application in automotive parts. In contrast, MoS_2 shows good thermal stability and, unlike MgO, possesses excellent mechanical properties. However, the thermal conductivity of MoS_2 is lower than that of MgO in the through-plane direction, 2 W/m·K while in-plane thermal conductivity of MoS_2 is 80–100 W/m·K. Considering the strengths and weaknesses of MgO and MoS_2, they were combined to form a core–shell structure providing excellent thermal and mechanical properties. MgO, displaying high thermal conductivity, was used as the core, and MoS_2, exhibiting low through-plane thermal conductivity, was synthesized as a nanosheet to create a shell surrounding the MgO to fabricate heat path using in-plane direction. The recent studies of core–shell structure/polymer composites indicated core–shell structure can easily enhance dielectric, mechanical or thermal properties of the composites [19–23]. Mixing the particles with this structure in a PPS matrix yielded a composite material with high thermal conductivity and improved mechanical performance.

2. Results and discussion

2.1. Elucidating the MgO@MoS_2 core–shell structure and surface treatment

The detailed experimental procedures, including the material synthesis and characterization, are provided in the Supplementary Information. The synthesis of the MgO@MoS_2 core–shell structure was verified using the X-ray diffraction (XRD), X-ray photoelectron spectroscopy (XPS) and field-emission scanning electron microscopy (FE-SEM) analyses, and the results are depicted in Fig. 1. The XRD pattern of MoS_2 demonstrates the synthesis of MoS_2 nanosheets without MgO particles, which agrees with the results of a previous study (PDF #37–1492) [24]. When the nanosheet structure has a few layers, the XRD pattern shows a broadening of the diffraction peaks. Characteristic peaks of the MoS_2 nanosheets are observed at 33°, 38°, and 59° corresponding to the (100), (103), and (110) planes, respectively. The XPS Mo 3d and S 2p spectra indicated the MoS_2 nanosheet was successfully synthesized. The Mo 3d5/2 peak at 229.5 eV indicated Mo elements was Mo(IV) ionic state with spin–orbit components of 3.15 eV and S 2p3/2 peak at 162.4 eV was also corresponding to previous reports about MoS_2 [25,26]. The FE-SEM image of MoS_2 (Fig. 1(d and e)) shows aggregated particles with various size ranges. While the synthesized MoS_2 particles did not seem sheet morphology, the high-resolution FE-SEM image reveals aggregated MoS_2 nanosheets with sizes in the range of 2–30 nm. In Fig. S1, the FE-SEM image, energy dispersive spectrometer (EDS) elemental mapping and energy dispersive X-ray spectroscopy (EDX) also indicate the MoS_2 nanosheets were successfully synthesized. The FE-SEM image (Fig. 1(f)) of MgO@MoS_2 core–shell structure shows MoS_2 sheet particles surrounding the MgO particles. Fig. S2 shows EDS elemental mapping and EDX of MgO@MoS_2 core–shell structure. The morphology of MoS_2 sheets was clearer and bigger than that of MoS_2 nanosheets which synthesized without MgO particles. In Fig. S3, the scanning transmission electron microscopy image and EDS elemental mapping indicated MgO particles aggregated forming core which can be distinguished as white region, and this can be also confirmed via EDS

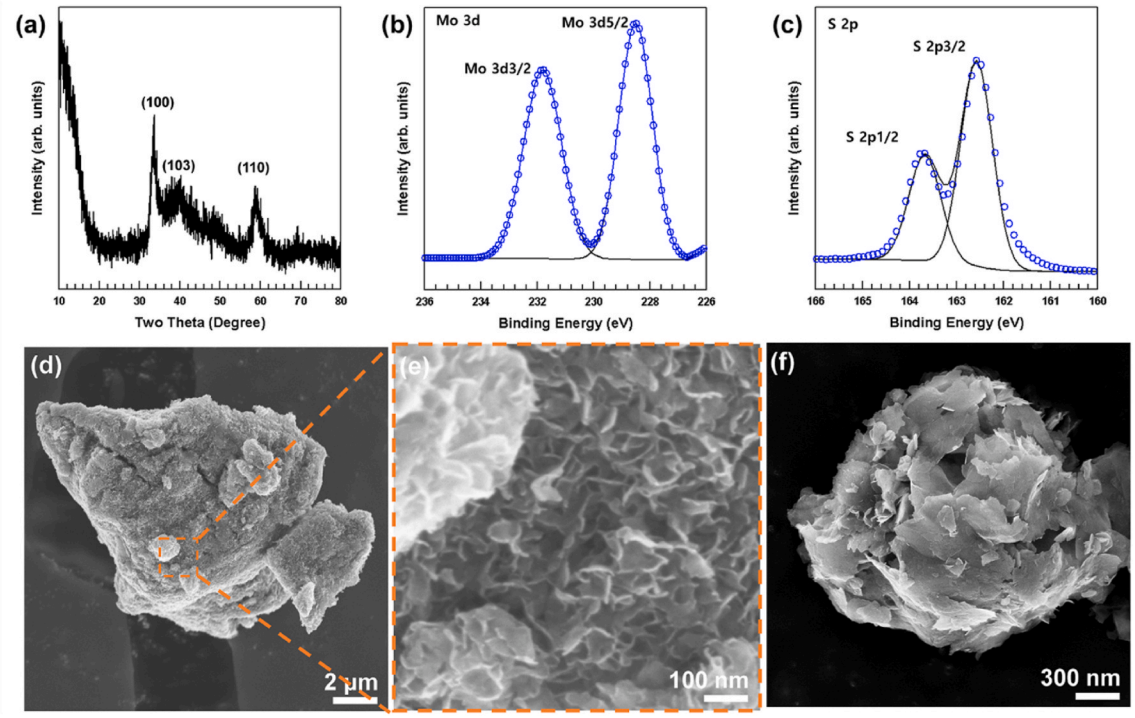


Fig. 1. (a) XRD pattern of synthesized MoS_2 nanosheets. High-resolution XPS spectrum of (b) Mo 3d and (c) S 2p of MoS_2 nanosheets. (d,e) FE-SEM image and high-resolution FE-SEM image of MoS_2 nanosheets (f) FE-SEM image of MgO@MoS_2 core–shell structure.

elemental mapping of field emission transmission electron microscopy. Mg and O elements are located in the center of the particle, and Mo and S elements appear to cover the Mg and O elements which can be seen as core–shell structure.

To confirm the MgO@MoS_2 core–shell structure, Fourier transform infrared spectroscopy (FT-IR) and thermogravimetric analysis (TGA) were performed. In Fig. 2(a), the FT-IR peaks at 615 and 1127 cm^{-1} are assigned to Mo–S vibrations [26,27]. The FT-IR peaks at 667, 553, and 409 cm^{-1} are the characteristic peaks of MgO. The FT-IR peak at 1639 cm^{-1} indicates an –OH bond attached to the MgO surface [28,29]. TGA was conducted to verify the mass ratio of MgO to MoS_2. The weight of MgO decreases gradually to 94%, whereas that of MoS_2 decreases to 87% at a temperature of up to 600 °C. The weight of the MgO@MoS_2 decreases to 92% owing to the thermal degradation of MoS_2 and then gradually reduces to 90%. During the synthesis, MgO particles were added to MoS_2 in a 5:3 wt ratio. The TGA results reveal a mass ratio of 4:3 for MoS_2 to MgO. Excess MoS_2 nanosheets were removed via centrifugation owing to their low weight. Further, the formation of core–shell structure is challenging at the MoS_2 to MgO weight ratio lower than 5:3, as shown in Fig. S4.

To enhance the attachment between the PPS matrix and MgO@-MoS_2, polyformaldehyde (polyoxymethylene; POM) and (3-aminopropyl)triethoxysilane (APTES) were coated on the MgO@MoS_2 core–shell structure (MgO@MoS_2/PA). The FT-IR and XPS analyses were performed to confirm the POM and APTES coating. The FT-IR peaks observed at 900 and 1035 cm^{-1} after coating could be attributed to the C–O bonds of POM and Si–O bonds of APTES, respectively [30–33]. In Fig. 3(b), XPS survey spectrum of MgO@MoS_2/PA indicated POM and APTES were successfully attached on the surface of MgO@-MoS_2 core–shell structure by presence of Si elements. From the XPS S 2p, Mg 2p and Mo 3d spectra, MgO and MoS_2 particles maintained their chemical bonding without any changes. The high-resolution XPS Si 2p spectrum in Fig. 3(f) shows the main peak properties of Si–O bonds after coating, and it is presumed that APTES is attached to the O of the POM to form Si–O bonds and due to Si–O bonding within the APTES structure [16]. The XRD pattern of MgO@MoS_2/PA (Fig. S5) resembles that of MgO@MoS_2 without any additional peaks, as POM and APTES show an amorphous structure. The Raman spectroscopy confirm that the coating process does not affect the chemical structure. Raman shifts at 398 and 375 cm^{-1} correspond to the peaks for MoS_2 [26,34], and those at 140 and 100 cm^{-1} could be assigned to the peaks of MgO [35,36], confirming that coating does not affect the MgO@MoS_2 chemical structure. TGA was conducted to verify the stability of MgO@MoS_2/PA at 300 °C, which is the temperature for composite fabrication using an extruder and injection molding process. In Fig. 3(h), Similar to that of the MgO@MoS_2 core–shell structure, less than 5% weight change is observed for MgO@MoS_2/PA up to a temperature of 300 °C, indicating their excellent stability at high temperatures. In Fig. S6, FE-SEM image and corresponding EDS elemental mapping and energy dispersive X-ray spectroscopy indicated the presence of POM and APTES on the surface of MgO@MoS_2.

2.2. Cross-sectional morphologies of PPS/MgO@MoS_2/PA composites and its mechanical tensile strength

The PPS composites with various filler ratio of MgO@MoS_2 and MgO@MoS_2/PA were fabricated via melting extrusion and then injection molding processes. The molten composite's viscosity becomes high with increasing filler ratio during extruding and injection molding, which is challenging to these processes. Therefore, the composites were fabricated up to a filler ratio of only 60%.

In the FE-SEM image of the PPS/MgO@MoS_2 composite (Fig. 4), The MgO@MoS_2 core-shell structure was maintained despite the high temperatures and pressures of the extrusion and injection molding processes. When the filler ratio was less than 40%, there was little difference in cross-sectional FE-SEM images. In Fig. S7, the cross-sectional FE-SEM images show MgO@MoS_2/PA particles were well randomly distributed. The FE-SEM images with high-resolution show without surface treatment, no adhesion is observed at the interfaces because there is no interaction between the PPS matrix and MgO@MoS_2. By contrast, when the surface is treated with POM and APTES, the amine functional groups of APTES interact with the PPS matrix via hydrogen bonding, which enables improved adhesion with the PPS matrix at the filler interfaces. In previous studies, the compatibility between ceramic filler treated with silane material and PPS matrix was improved, resulting in improved thermal conductivity and mechanical strength [10,16,37]. As the filler ratio increases over 40%, MgO@MoS_2 particles without surface treatment started to aggregate each other while MgO@MoS_2/PA particles were well randomly distributed. The aggregation of untreated filler affected to mechanical and thermal properties.

The differences in the universal testing machine (UTM) results are attributed to the difference in attachment between the PPS matrix and the MgO@MoS_2/PA filler as shown in Fig. 5(a). The pristine PPS matrix exhibits a tensile strength of 60 MPa, which agrees with the results of previous research [10,16,38]. With increasing filler ratio, the tensile strength gradually increases up to 82 and 85 MPa for a filler ratio of 40%

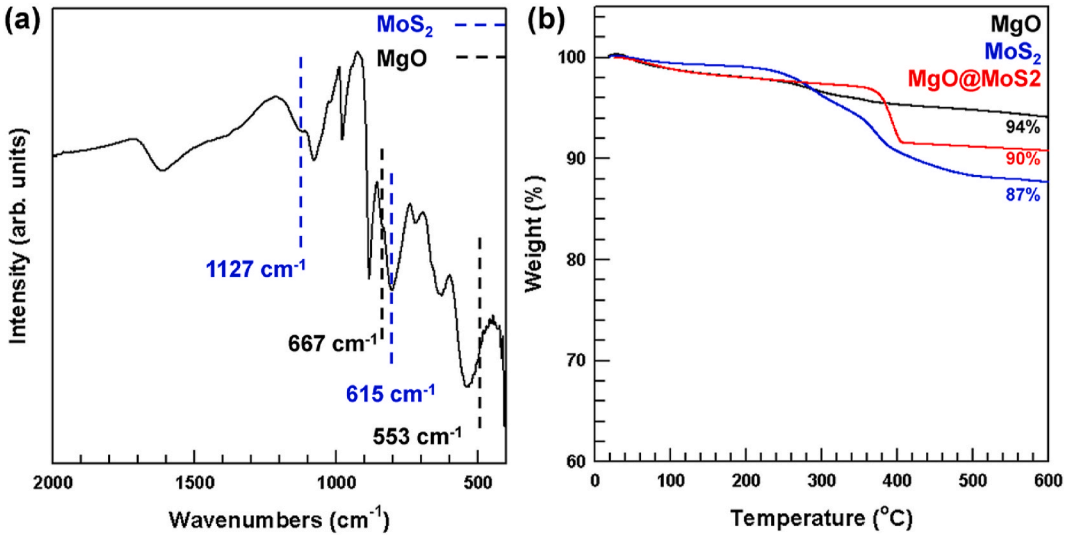


Fig. 2. (a) FT-IR spectrum of MgO@MoS_2 core–shell structure. (b) TGA results of MgO, MoS_2 and MgO@MoS_2 core–shell structure.

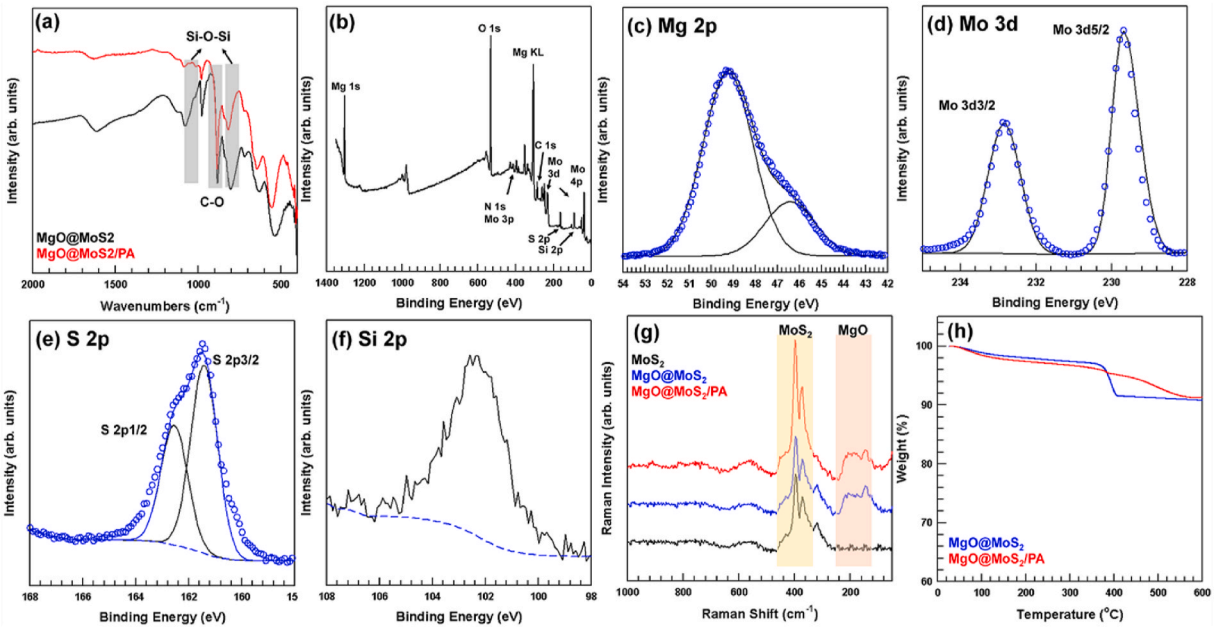


Fig. 3. (a) FT-IR spectrum of MgO@MoS_2 and MgO@MoS_2/PA. (b) XPS survey spectrum of MgO@MoS_2/PA. High-resolution XPS spectrum of (c) Mg 2p (d) Mo 3d (e) S 2p and (f) Si 2p of MgO@MoS_2/PA. (g) Raman spectrum of MoS_2, MgO@MoS_2, MgO@MoS_2/PA. (h) TGA results of MgO@MoS_2 and MgO@MoS_2/PA

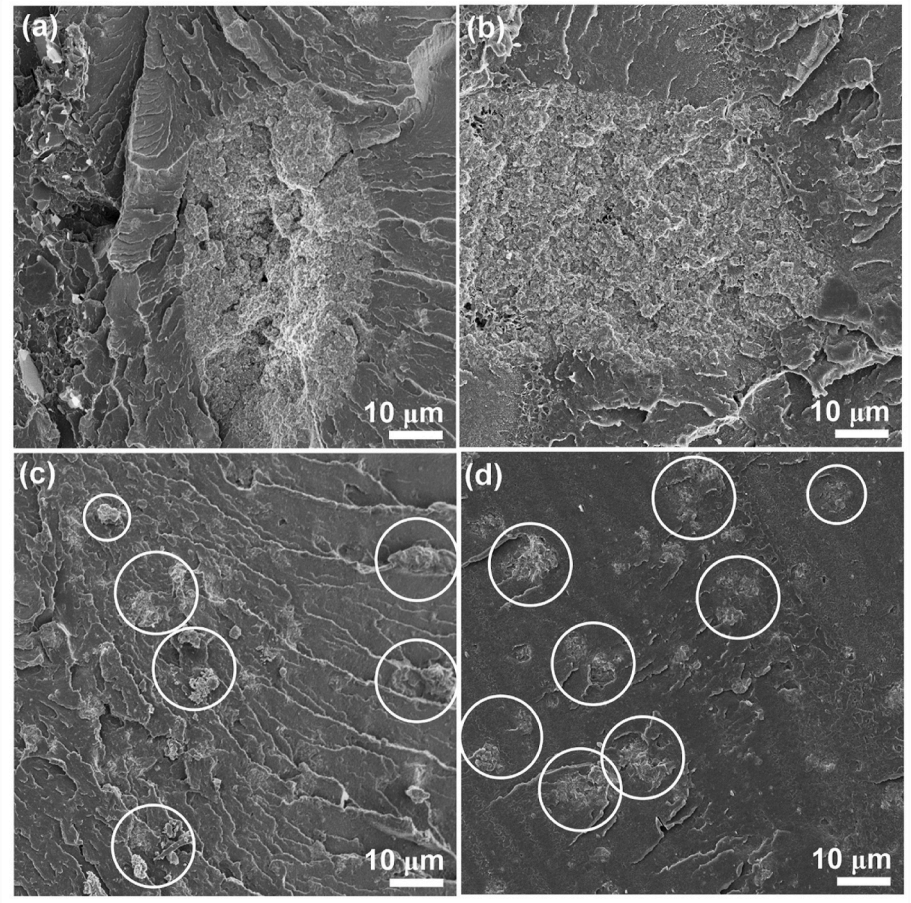


Fig. 4. (a) Cross-sectional FE-SEM images of (a) 50% PPS/MgO@MoS_2 composite (b) 60% PPS/MgO@MoS_2 composite (c) 50% PPS/MgO@MoS_2/PA composite and (d) 60% PPS/MgO@MoS_2/PA composite.

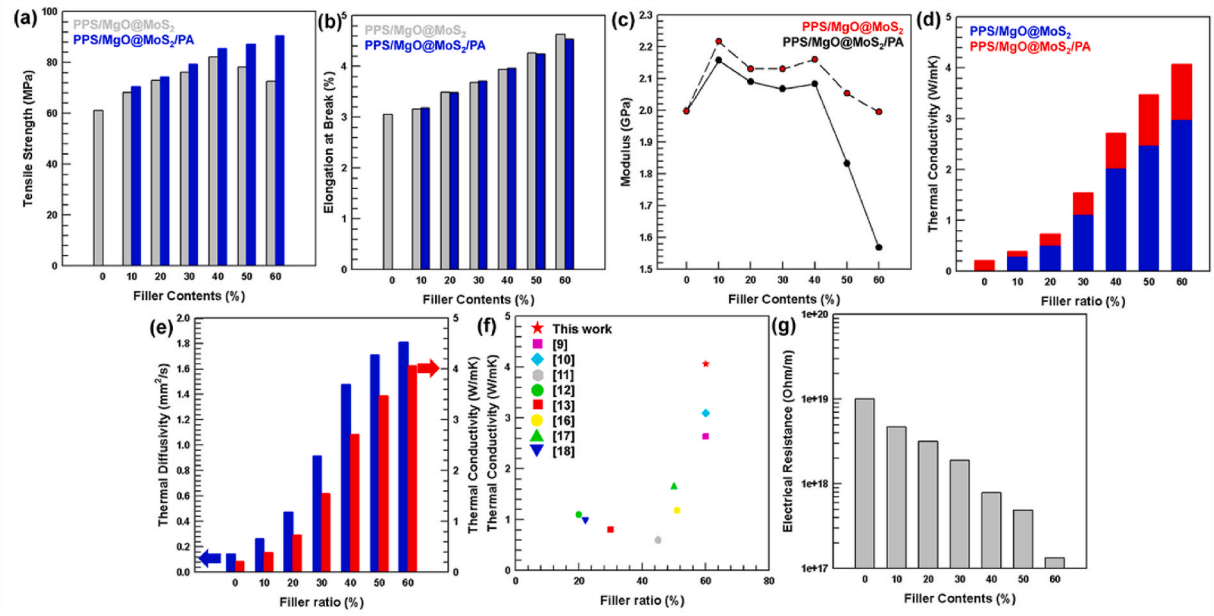


Fig. 5. (a) Tensile strength, (b) Elongation at break, Young's modulus and (d) Thermal conductivity of PPS/MgO@MoS_2 composites with increasing filler contents. (e) Thermal diffusivity and thermal conductivity of PPS/MgO@MoS_2/PA composites. (f) Through-plane thermal conductivity versus filler fraction of PPS/MgO@-MoS_2/PA composites in comparison with other thermal conductive composites. (g) Electrical resistance of PPS/MgO@MoS_2/PA composites with increasing filler contents.

without and with surface treatment, respectively. When the filler ratio was less than 40%, the PPS matrix phase distribution of MgO@MoS_2/PA filler and MgO@MoS_2 filler was similar without agglomeration, so the tensile strength was improved without significant difference. However, when the filler ratio exceeds 40%, the MgO@MoS_2 particles aggregate, increasing cracks in the PPS matrix and decreasing tensile strength for PPS/MgO@MoS_2 composites. In PPS/MgO@MoS_2/PA composites, surface treatment with POM and APTES facilitates the dispersion of fillers in the PPS matrix and increases the interfacial attachment between PPS matrix and MgO@MoS_2 fillers, resulting in an increase in tensile strength to 90 MPa. By adding MgO@MoS_2 or MgO@MoS_2/PA fillers, like tensile strength, the elongation at break increased. However, PPS has very low elongation at break value of 3 %, elongation at break of both PPS/MgO@MoS_2 and PPS/MgO@MoS_2/PA composites was up to 5 %. The Young's modulus of the samples determined from the slope of the stress–strain curve. Up to 40 % filler contents, modulus of both composites increased compared to neat PPS. However, 50 and 60 % filler contents composites showed difference. The Young's modulus of PPS/MgO@MoS_2 composite decreased sharply, while that of PPS/MgO@MoS_2/PA decreased slightly. This difference may be due to the aggregation of MgO@MoS_2 filler as shown in Fig. 4.

2.3. Thermal properties of the PPS/MgO@MoS_2/PA composites

Both MgO and MoS_2 exhibit high thermal conductivity, showing values between 30 and 60 W/m·K and 80–100 W/m·K which is in-plane thermal conductivity for MoS_2 sheets, respectively, whereas the PPS matrix displays poor thermal conductivity with a value of 0.18 W/m·K. Fig. 5(b) shows the thermal conductivities of the composites measured in the vertical direction for various filler ratios. As the filler ratio of PPS/MgO@MoS_2/PA composites increases to 60%, the thermal conductivity increases to 4.07 W/m·K while thermal conductivity of PPS/MgO@-MoS_2 composites was only 2.91 W/m·K. Surface treatment with POM and APTES improves the adhesion between PPS and MgO@MoS_2/PA, thereby improving the dispersibility of the filler, which facilitates the formation of a heat conduction path, enhancing the thermal conductivity compared to that without surface treatment. Due to the non-uniform arrangement of fillers in the composite and low interface adhesion with the PPS matrix, the thermal conductivity was lower than that of PPS/MgO@MoS_2 composites. The increase of thermal diffusivity of the PPS/MgO@MoS_2 composites is a main factor for achieving high thermal conductivity. According to recently reported results of PPS composites as shown in Fig. 5(d), our PPS/MgO@MoS_2/PA composites show high thermal conductivity.

Additionally, the electrical resistivity of PPS/MgO@MoS_2/PA was evaluated in Fig. 5(e), because MoS_2 is an electrically conductive material. The electrical resistivities of the composites were measured using a four-point probe instrument. Because PPS and MgO are insulating materials, the electrical resistances of all composites are high, and they are considered insulators, although MoS_2 is a conductive material. Furthermore, PPS composites have to maintain an insulating state for application in the automobile industry. Insulation is essential because non-insulated electric vehicle parts can result in severe problems such as fire, electric shock, or electric leakage due to the high battery voltage.

3. Conclusions

In this study, we fabricated PPS-based composites with high thermal conductivities and improved mechanical properties. MgO and MoS_2 nanosheets formed core–shell structures, and the surfaces were treated with POM and APTES to improve the interfacial adhesion between the PPS and the MgO@MoS_2 filler. The core–shell structure and surface treatment were confirmed via XRD, XPS, Raman spectroscopy, TGA, FT-IR, and FE-SEM analyses. The fabrication of PPS/MgO@MoS_2/PA composites demonstrated the challenges associated with a high filler content, which affects the viscosity during the extrusion and molding processes. Surface treatment played a crucial role in improving the attachment between the PPS matrix and the MgO@MoS_2/PA filler, although particle breakage is observed at higher filler ratios. The mechanical properties of the composites revealed that the tensile strength gradually increased with the increasing filler ratio of up to 40%. Subsequently, the MgO@MoS_2 particle aggregation reduced the tensile strength. Surface treatment mitigated this effect, resulting in a relatively minor reduction in the tensile strength of the MgO@MoS_2/PA composites. Thermal conductivity assessments revealed a considerable improvement in the composites with increased filler content, attributed

to the formation of heat paths. The surface treatment further enhanced the thermal conductivity. Electrical resistivity measurements demonstrated that the composites maintained an insulating state, crucial to their application in EVs and other industries. Therefore, the systematic characterization and modification of MgO@MoS_2 nanosheets combined with the surface treatment of PPS/MgO@MoS_2/PA composites provided valuable insights into their behavior, and a considerable improvement in their structural, mechanical, and thermal properties, makes them promising candidates for various engineering applications, particularly in the automotive industry.

Declaration of competing interest

The authors declare that they have no known competing financial interests or personal relationships that could have appeared to influence the work reported in this paper:Declarations of interest: none.

Acknowledgement

This research was supported by the Industrial Technology Innovation Program (20011165) funded by the Ministry of Trade, Industry & Energy (MOTIE, Korea) and supported by the Human Resources Development (No. 20214000000280) of the Korea Institute of Energy Technology Evaluation and Planning (KETEP) grant funded by the Korea government Ministry of Trade, Industry and Energy.

Appendix A. Supplementary data

Supplementary data to this article can be found online at https://doi.org/10.1016/j.jmrt.2024.06.021.

References

[1] Jang K-S. Mechanics and rheology of basalt fiber-reinforced polycarbonate composites. Polymer 2018;147:133–41.
[2] Kausar A. A review of filled and pristine polycarbonate blends and their applications. J Plast Film Sheeting 2018;34:60–97.
[3] Francisco DL, Paiva LB, Aldeia W. Advances in polyamide nanocomposites: a review. Polym Compos 2019;40:851–70.
[4] García JM, García FC, Serna F, de la Peña JL. High-performance aromatic polyamides. Prog Polym Sci 2010;35:623–86.
[5] Fabbri P, Bassoli E, Bon SB, Valentini L. Preparation and characterization of poly (butylene terephthalate)/graphene composites by in-situ polymerization of cyclic butylene terephthalate. Polymer 2012;53:897–902.
[6] Joshi M, Misra A, Maiti S. Polybutylene terephthalate/high-density polyethylene alloys. I. Morphological studies. J Appl Polym Sci 1991;43:311–28.
[7] Janik H, Marzec M. A review: fabrication of porous polyurethane scaffolds. Mater. Sci. Eng. C. 2015;48:586–91.
[8] Moulay S. Chemical modification of poly (vinyl chloride)—still on the run. Prog Polym Sci 2010;35:303–31.
[9] Gu J, Guo Y, Yang X, Liang C, Geng W, Tang L, Li N, Zhang Q. Synergistic improvement of thermal conductivities of polyphenylene sulfide composites filled with boron nitride hybrid fillers. Compos. Part A Appl Sci Manuf 2017;95:267–73.
[10] Ryu S, Kim K, Kim J. Silane surface modification of boron nitride for high thermal conductivity with polyphenylene sulfide via melt mixing method. Polym Adv Technol 2017;28:1489–94.
[11] Zhao J, Cai S, Chen X, Ren H, Yan Y. Preparation and properties of boron nitride or aluminum nitride reinforced glass fiber/modified polyphenylene sulfide composites. Adv Polym Technol 2023:2023.
[12] Kim M, Park S, Park J. Effect of the grafting reaction of aluminum nitride on the multi-walled carbon nanotubes on the thermal properties of the poly (phenylene sulfide) composites. Polymers 2017;9:452.
[13] Guo B, Lin Q, Zhao X, Zhou X. Crystallization of polyphenylene sulfide reinforced with aluminum nitride composite: effects on thermal and mechanical properties of the composite. Iran Polym J (Engl Ed) 2015;24:965–75.
[14] Gu J, Xie C, Li H, Dang J, Geng W, Zhang Q. Thermal percolation behavior of graphene nanoplatelets/polyphenylene sulfide thermal conductivity composites. Polym Compos 2014;35:1087–92.
[15] Wu Y, Liu Q, Heng Z, Zou H, Chen Y, Liang M. Improved mechanical properties of graphene oxide/short carbon fiber–polyphenylene sulfide composites. Polym Compos 2019;40:3866–76.
[16] Kim M, Cho Y, Yang W, Kim J. Improved thermal conductivity of poly (p-phenylene sulfide)/glass fiber composites via addition of polysiloxide-coated aggregated boron oxide and silane-treated graphene oxide. Mater Chem Phys 2023;302:127737.
[17] Tantug GS, Seki Y, Sarikanat M, Altay L, Gulen S, İsbilir A. Thermal conductivity and mechanical properties of synthetic graphite loaded polyphenylene sulfide composites. AIP Conf Proc 2020;2205:020033.
[18] Shi Y, Bai Y, Lei Y, Zhang H, Zhou S, Zou H, Liang M, Chen Y. Simultaneously enhanced heat dissipation and tribological properties of polyphenylene sulfide-based composites via constructing segregated network structure. J Mater Sci Technol 2022;99:239–50.
[19] Zhang Y, Zhou W, Peng W, Yao T, Zhang Y, Wang B, Cai H, Li B. Core@ double–Shell engineering of Zn particles toward elevated dielectric properties: multiple polarization mechanisms in Zn@ Znch@ PS/PVDF composites. Macromol Rapid Commun 2024;45(4):2300585.
[20] Wang F, Zhou W, He Y, Lv Y, Wang Y, Wang Z. Synergetic improvement of dielectric properties and thermal conductivity in Zn@ ZnO/carbon fiber reinforced silicone rubber dielectric elastomers. Compos. -A: Appl. Sci. Manuf. 2024;181:108129.
[21] Chen X, Zhou W, Wang F, Wu H, Zhong S, Li B. Meliorative dielectric properties in core@ double-shell structured Al@ Al2O3@ PDA/PVDF nanocomposites via decoupling the intra-particle polarization and inter-particle polarization. Mater Today Energy 2024;41:101543.
[22] Zhou W, Li X, Zhang F, Zhang C, Li Z, Chen F, Cai H, Liu X, Chen Q, Dang Z-M. Concurrently enhanced dielectric properties and thermal conductivity in PVDF composites with core-shell structured β-SiCw@ SiO2 whiskers. Compos. -A: Appl. Sci. Manuf. 2020;137:106021.
[23] Xia L, Wang X, Guo C, Miao Z, Dai J, Li D, Xu Y, Luo W, Yuan C, Zeng B, Dai L. Core-shell structured ZnO nanorods enable flame-retardant, smoke suppressed and mechanically reinforced epoxy resin composites. Compos Commun 2022;35:101311.
[24] Singh MK, Chettri P, Tripathi A, Tiwari A, Mukherjee B, Mandal R. Defect mediated magnetic transitions in Fe and Mn doped MoS 2. Phys Chem Chem Phys 2018;20:15817–23.
[25] Sarma S, Ghosh B, Ray SC, Wang H, Mahule T, Pong W. Electronic structure and magnetic behaviors of exfoliated MoS2 nanosheets. J Phys Condens Matter 2019;31:135501.
[26] Ma H, Shen Z, Ben S. Understanding the exfoliation and dispersion of MoS2 nanosheets in pure water. J Colloid Interface Sci 2018;517:204–12.
[27] Ahmad S, Khan I, Husain A, Khan A, Asiri AM. Electrical conductivity based ammonia sensing properties of polypyrrole/MoS2 nanocomposite. Polymers 2020;12:3047.
[28] Imani MM, Safaei M. Optimized synthesis of magnesium oxide nanoparticles as bactericidal agents. J. Nanotechnol 2019:2019.
[29] Balraj B, Senthilkumar N, Potheher IV, Arulmozhi M. Characterization, antibacterial, anti-arthritic and in-vitro cytotoxic potentials of biosynthesized magnesium oxide nanomaterial. Mater Sci Eng B 2018;231:121–7.
[30] Lu B, Bai B, Zhang R, Ma J, Mao L, Shi J, Jin H. Study on gasification characteristics and kinetics of polyformaldehyde plastics in supercritical water. J Clean Prod 2023;383:135459.
[31] Kang X, Liu Y, Chen N, Feng W, Liu B, Xu Y, Li J, Ding T, Fang X. Influence of modified ammonium polyphosphate on the fire behavior and mechanical properties of polyformaldehyde. J Appl Polym Sci 2021;138:50156.
[32] Coombs SG, Khodjaniyazova S, Bright FV. Exploiting the 3-Aminopropyltriethoxysilane (APTES) autocatalytic nature to create bioconjugated microarrays on hydrogen-passivated porous silicon. Talanta 2018;177:26–33.
[33] Isasi J, Arévalo P, Martin E, Martín-Hernández F. Preparation and study of silica and APTES–silica-modified NiFe 2 O 4 nanocomposites for removal of Cu 2+ and Zn 2+ ions from aqueous solutions. J Sol Gel Sci Technol 2019;91:596–610.
[34] Zhao Y, Sun Y, Bai M, Xu S, Wu H, Han J, Yin H, Guo C, Chen Q, Chai Y. Raman spectroscopy of dispersive two-dimensional materials: a systematic study on MoS2 solution. J Phys Chem C 2020;124:11092–9.
[35] Zhang Y, Li H, Liu S, Wu N, OuYang S. Raman spectroscopic study of irregular network in the process of glass conversion to CaO-MgO-Al2O3-SiO2 glass-ceramics. J Non-Cryst Solids 2021;563:120701.
[36] Daoudi K, El-Helali S, Othmen Z, Suleiman B, Tsuchiya T. Microstructure and electrical transport mechanisms of the Ca-doped LaMnO3 films grown on MgO substrate. J. Materiomics 2020;6:17–23.
[37] Zhang R, Liang F, Zeng Y, Yang C, Wu Z. Properties of polyphenylene sulphide/glass fibre composites with negative thermal expansion ceramic fillers. Ceram. Inter. 2023;49(18):29639–46.
[38] Gao Y, Fu Q, Niu L, Shi Z. Enhancement of the tensile strength in poly (p-phenylene sulfide) and multi-walled carbon nanotube nanocomposites by hot-stretching. J Mater Sci 2015;50:3622–30.